Journal of Materials Chemistry A

ROYAL SOCIETY OF CHEMISTRY

PAPER

View Article Online
View Journal | View Issue

Cite this: J. Mater. Chem. A, 2023, 11, 7505

Alloying promotion of Pd-based metallenes in electrocatalytic hydrogenation of functionalized nitroarenes†

Wenbiao Zhang,[ab] Wanling Zhang,[a] Jingwen Tan,[a] Di Pan,[b] Yi Tang *[b] and Qingsheng Gao *[a]

Received 27th December 2022
Accepted 1st March 2023

DOI: 10.1039/d2ta10021e

rsc.li/materials-a

Electrocatalytic hydrogenation (ECH) provides a controllable and sustainable reduction of organic compounds *via* multi-electron-transfer processes under ambient conditions, which urgently demands high-performance electrocatalysts with satisfactory activity and selectivity. Here, two-dimensional Pd-based metallenes are for the first time introduced as efficient electrocatalysts for the ECH of nitroarenes, showing the intrinsic promotion of active sites by alloying effects. Thereinto, a Pd–Mo metallene with a highly exposed active surface and strong electronic interactions between Pd and Mo atoms affords the chemoselective hydrogenation of 4-nitrostyrene (4-NS) toward value-added 4-vinylaniline (4-VA). At −0.25 V *vs.* RHE, it reaches a high selectivity (>90.0%) and faradaic efficiency (78.3%) of 4-VA, outperforming the counterparts of a home-made Pd metallene and commercial Pd/C. The consistent alloying promotion is further verified on a series of Pd–M (M = Cr, Mo, and W) metallenes, with the specific activity sequence (Pd–Mo > Pd–W > Pd–Cr > Pd) that can be theoretically interpreted by the gradually strengthened chemisorption of 4-NS after alloying Pd with M. Moreover, the good efficiency within a broad substrate scope highlights the promise of Pd-based metallenes in electrochemical refinery.

Introduction

Avoiding harsh operations associated with high temperature and H_2 pressure, electrocatalytic hydrogenation (ECH) guarantees the hydrogenation of unsaturated functional groups (*e.g.*, carbonyl, nitro, alkenyl, *etc.*) under ambient conditions with sustainable electricity as the driving energy and water as the hydrogen source.[1–4] For example, the hydrogenation of nitroarenes to aniline derivatives, a key process for manufacturing medicine, dyes, spices, and other chemicals,[5–7] is challenged by the trade-off between activity and selectivity in thermo-catalysis owing to the difficult control over pathways under heated and pressurized conditions.[8,9] ECH enables a more controllable alternative to accommodate such multi-electron transfer processes *via* the convenient and accurate modulation of potential or current on working electrodes.[8,10,11] Thereinto, electrocatalysts with elaborately designed surface configurations usually play a paramount role in promoting an efficient transformation *via* target routes.[12–15]

Palladium (Pd)-based electrocatalysts capable of adsorbing/activating protons and water are highly active for cathodic hydrogenation.[16–20] Unfortunately, they are also active for the hydrogen evolution reaction (HER) that consumes chemisorbed H (H*, * denotes an active site) and reduces the faradaic efficiencies (FEs) of target aniline products.[21] Moreover, the target reduction of nitro to amido in a complete manner, which avoids the formation of nitrosobenzene, phenylhydroxylamine, azoxybenzene, and hydrazobenzene, but retains other reducible groups well (*e.g.*, C=C, C≡C, –F/Cl/Br/I, *etc.*),[14,22,23] highly requires the atomic-level modulation on nanostructured Pd to optimize the chemisorption of substrates and intermediates. Recently, two-dimensional (2D) metallenes have attracted extensive interest in a variety of electrocatalysis reactions (*e.g.*, oxygen/nitrogen/water reduction, alcohol oxidation, CO_2 reduction, *etc.*) due to the largely exposed active surface and more importantly the tunable intrinsic activity after alloying with foreign elements.[24–33] These features would not only ensure the feasible manipulation of reactant/intermediate chemisorption toward target ECH but also provide a reliable platform with well-defined atomic arrangements and electronic configurations to unravel the electrocatalytic mechanism.[30,34] However, the relevant knowledge is still absent in the ECH of nitroarenes.

[a]College of Chemistry and Materials Science, Guangdong Provincial Key Laboratory of Functional Supramolecular Coordination Materials and Applications, Jinan University, Guangzhou 510632, P. R. China. E-mail: tqsgao@jnu.edu.cn

[b]Department of Chemistry, Shanghai Key Laboratory of Molecular Catalysis and Innovative Materials, Laboratory of Advanced Materials and Collaborative Innovation Centre of Chemistry for Energy Materials, Fudan University, Shanghai 200433, China. E-mail: yitang@fudan.edu.cn

† Electronic supplementary information (ESI) available: EDS mapping, additional XRD, XPS and CVs, and DFT calculation details. See DOI: https://doi.org/10.1039/d2ta10021e

In this work, Pd-based metallenes are for the first time introduced as efficient electrocatalysts for the ECH of nitroarenes. Featuring highly exposed surface and strong electronic interactions between Pd and Mo atoms, ultrathin Pd–Mo (thickness ~3 nm) affords the chemoselective hydrogenation of 4-nitrostyrene (4-NS) to value-added 4-vinylaniline (4-VA) in a wide potential range of −0.05 to −0.45 V *vs.* RHE. At −0.25 V *vs.* RHE, it reaches a high selectivity (>90.0%) and faradaic efficiency (78.3%) of 4-VA, superior to the Pd metallene and commercial Pd/C counterparts. The consistent alloying promotion is further verified on a series of Pd–M (M = Cr, Mo, and W) metallenes, whose specific activity for hydrogenating 4-NS follows the sequence of Pd–Mo > Pd–W > Pd–Cr > Pd. Accordingly, density functional theory (DFT) calculations show that alloying with foreign M atoms can effectively ameliorate electronic configurations to strengthen the chemisorption of 4-NS, which is conducive to the electrochemical hydrogenation toward anilines *via* the facilitated H* transfer to activated nitro groups, rather than gaseous H_2 evolution. This calculation gives a coincidental correlation between the specific activity and surface binding energy on Pd-based metallenes, confirming the alloying promotion of ECH within a broad substrate scope.

Experimental section

Chemicals

4-Nitrostyrene (4-NS, 97%), 4-vinylaniline (4-VA, 99%), 4-ethylaniline (4-EA, 99%) and 4-ethylnitrobenzene (4-EN, 99%), molybdenum hexacarbonyl ($Mo(CO)_6$, 98%) and oleylamine (80–90%) were purchased from Macklin Inc. Shanghai. Ascorbic acid (AR) and $LiClO_4$ (AR) were provided by Aladdin Inc. Shanghai, and palladium acetylacetonate ($Pd(ac)_2$, 95%) was bought from Meryer Co., LTD. All reagents were used directly without any treatments.

Synthesis of Pd-based metallenes

In a typical synthesis of the Pd–Mo metallene,[24] 5 mL of oleylamine was used to dissolve $Pd(ac)_2$ (12 mg), $Mo(CO)_6$ (4 mg), and ascorbic acid (30 mg) in a 25 mL glass round-bottom flask immediately followed by ultrasonication for 30 min. The obtained homogeneous solution was then sealed and heated in an oil bath at 80 °C for 12 h with stirring and then naturally cooled to room temperature. Residual oleylamine was washed with an ethanol–cyclohexane mixture. The colloidal material was stored in cyclohexane for later use. The synthesis of Pd–W and the Pd–Cr samples was conducted in the same manner except that $Mo(CO)_6$ was replaced by $W(CO)_6$ and $Cr(CO)_6$, respectively.

The Pd metallene was synthesized through the above wet-chemical method replacing $Mo(CO)_6$ with CO gas. 5 mL of oleylamine was used to dissolve $Pd(ac)_2$ (12 mg) and ascorbic acid (30 mg), followed by ultrasonication until a homogeneous solution was acquired. The solution was then placed into a Teflon high-pressure vessel saturated with CO gas and then heated at 80 °C for 12 h. Products were collected by centrifugation and washed with a mixture of ethanol–cyclohexane, which was then stored in cyclohexane (10 mg mL^{-1}) for use.

Physical characterization

X-ray diffraction (XRD) patterns were collected on a Bruker D8 Advance diffractometer (Cu Kα radiation, λ = 0.154 nm). Transmission electron microscopy (TEM) and high-angle annular dark-field scanning TEM (HAADF-STEM) images were acquired on a JEOL JEM-2100F electron microscope. Scanning electron microscopy (SEM) was performed on a ZEISS ULTRA 55. X-ray photoelectron spectroscopy (XPS) was performed on a ThermoFisher scientific (Escalab 250Xi) using C 1s (284.6 eV) as a reference. The contents of metal elements in metallenes were detected by using an inductively coupled plasma-optical emission spectrometer (ICP-OES, OPTIMA 2000DV). Atomic-force microscopy (AFM, Bruker Innova) was employed to explore the morphologies of the surface in tapping mode.

Electrochemical test

The Pd-based metallene colloid kept in cyclohexane (10 mg mL^{-1}, 100 μL) was loaded onto a carbon cloth (1 cm × 2 cm) and dried naturally to reach a mass loading of 0.25 mg cm^{-2}. Afterwards, 10 μL Nafion 115 (5 wt%) solution was transferred onto the electrode surface. To access the reliable electrolysis on the clean surface of Pd-based alloys free from interference by adsorbed surfactants, the metallene was at first electrochemically cleaned by repeated cyclic voltammograms (CVs) in 1 M KOH.[35,36] Typically, a metallene-loading working electrode was swept at 50 mV s^{-1} in N_2-saturated solution (1.0 M KOH) for 40 cycles (−0.8 to 0.3 V *vs.* SCE), with a standard calomel electrode (SCE) and Pt foil as the reference and counter electrodes, respectively. Next, the electrode was removed and washed with ultrapure water and ethanol for later tests.

The ECH of 4-NS to 4-VA was performed in an airtight two-compartment electrochemical cell separated by a proton exchange membrane (Nafion 117, Sigma-Aldrich). The electrolyte was 45 mL $LiClO_4$ solution (pH 6.8) containing 15 mmol L^{-1} of 4-NS in a cathodic cell. Each compartment contained approximately 10 mL headspace. N_2 gas was passed into the cathodic compartment electrolyte for at least 30 min to strip the dissolved air before the test. During the test, a N_2 gas flow (35 mL min^{-1}) was delivered into the cathodic chamber and then vented into the gas-sampling loop of a gas chromatograph (GC). Linear sweep voltammetry (5 mV s^{-1}) was conducted on a CHI 660e potentiostat (CH Instruments), using a SCE and a graphite rod as the reference and counter electrodes, respectively. The working potentials in ECH were calibrated to the reversible hydrogen electrode (RHE), according to Nernst equations.

Product analysis

The H_2 and the liquid products were measured by GC and high-performance liquid chromatography (HPLC), respectively. GC (FULI 9790) equipped with a gas sample loop was employed to quantify the H_2 gas produced by the HER every 30 min, and N_2 (99.99%) was the carrier gas. The FE of H_2 production was calculated from the GC results as below:

$$FE_{(H_2)} = \frac{\text{peak area of } H_2 \times \text{flow rate} \times z \times F \times t}{\alpha \times V_m \times Q}$$

where α is the conversion factor for H_2 based on calibration of GC with a standard sample, $z = 2$ (transferred electrons), t is the total reaction time, Q is the total charge passed, $V_m = 22.4$ L mol^{-1}, and $F = 96\,485$ C mol^{-1}.

Liquid products in the cathode electrochemical cell were analysed using a HPLC (SHIMADZU LC-20AT) system equipped with a UV detector. The column (INERTSUSTAIN C18) was operated at 40 °C and the binary gradient method containing H_2O and CH_3OH (CH_3OH: 60 vol%) was adopted at a flow rate of 0.8 mL min^{-1}. The conversion (%) of reactants, the selectivity (%) and yield (%) of products, and the efficiency (%) of hydrogenation products were calculated based on the following equations:

$$\text{Conversion } (\%) = \frac{\text{mole of product}}{\text{mole of initial substrate}} \times 100\%$$

$$\text{Selectivity } (\%) = \frac{\text{mole of target product}}{\text{mole of total products}} \times 100\%$$

$$\text{Yield } (\%) = \frac{\text{mole of product}}{\text{mole of theoretical product}} \times 100\%$$

$$\text{FE } (\%) = \frac{\text{mole of product} \times z \times F}{\text{total charge used}} \times 100\%$$

where z, the number of transferred electrons, was 6 for 4-VA and 8 for 4-ethylaniline (4-EA) products.

Theoretical calculations

DFT calculations were performed at the GGA level within the Perdew–Burke–Ernzerhof (PBE) functional using the CASTEP software implemented in Materials Studio. The total energy calculation was performed using a kinetic energy cutoff of 450.0 eV assigned to the plane-wave basis set for calculating the density of states. The self-consistent field (SCF) tolerance was 1×10^{-6} eV. The Brillouin zone was sampled using $5 \times 5 \times 1$ k-points. The core electrons were replaced with ultrasoft pseudopotentials. All Pd–M structures for calculation were the commonly observed (111) facet of face-centred cubic (*fcc*) structure materials and were modeled with vacuum widths of 12 Å, using a five-layer 2×2 surface slab. Pd–M (M = Mo, W, and Cr) structures were established by replacing one of the *hcp*-Pd atom by M in the $2 \times 2 \times 2$ supercell.

The binding energy (BE) of H and 4-NS was obtained from:[37]

$$BE_{(adsorbate)} = E_{(slab+adsorbate)} - E_{(slab)} - E_{(adsorbate)}$$

in which $E_{(slab+adsorbate)}$, $E_{(slab)}$ and $E_{(adsorbate)}$ are the total energy of Pd–M surface with adsorbates, the energy of the pure surface/facet, and the energy of gaseous adsorbates, respectively. The $E_{(H)}$ was taken as half the total energy of the H_2 molecule during the calculation of hydrogen binding energy.

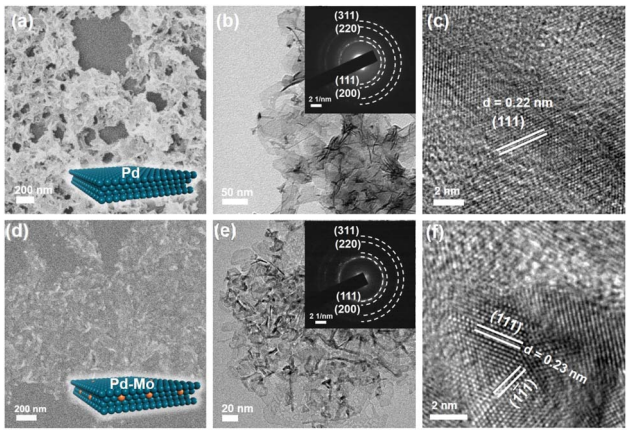

Fig. 1 (a and d) SEM, (b and e) TEM, and (c and f) HR-TEM images of (a–c) Pd and (d–f) Pd–Mo metallenes. Insets of (b) and (e) display the SAED images.

Results and discussion

The Pd–Mo metallene was synthesized *via* a one-pot wet-chemical approach,[24] as mentioned in the Experimental section. For reference, the monometallic Pd metallene was obtained *via* the consistent procedure except replacing $Mo(CO)_6$ with CO. Their SEM images (Fig. 1a and d) showed flower-like products composed of 2D nanosheets, which was further confirmed using the corresponding TEM images in Fig. 1b and e. The selective area electronic diffraction (SAED) patterns suggested the polycrystal nature of both Pd–Mo and Pd metallenes (insets of Fig. 1b and e). The high-resolution TEM (HR-TEM) image of the Pd–Mo metallene clearly depicted a lattice spacing of 0.23 nm (Fig. 1f), slightly larger than the Pd(111) (0.22 nm) observed in Pd counterparts (Fig. 1c). This should be ascribed to the lattice expansion after alloying Pd with relatively larger Mo atoms. Accordingly, HAADF-STEM and the elemental mapping confirmed the homogenous distribution of Pd and Mo throughout the nanosheets (Fig. S1, ESI†), and the atomic ratio of Mo/Pd was 0.03. The further quantification by ICP-OES showed the Mo content of 3.1 wt% in Pd–Mo, suggesting a consistent Mo/Pd molar ratio of 0.04 (Table S1, ESI†). Interestingly, the Mo/Pd ratio remained at the same level (0.03–0.04) in a series of 2D nanostructured Pd–Mo samples received after varying the feeding content of $Mo(CO)_6$ from 2 to 15 mg along with the fixed one of $Pd(ac)_2$ (12 mg) (Fig. S2 and Table S2, ESI†). This should be associated with the crystalline nature of Pd–Mo alloys, and excessive Mo during preparation is residual in the reaction solution.

XRD investigation identified the same *fcc* structure of both Pd and Pd–Mo metallenes (Fig. 2a). But the diffraction peaks of Pd–Mo were negatively shifted to lower 2θ compared to those of the Pd metallene and commercial Pd/C, indicating the formation of alloys with expanded lattices. XPS further revealed that Pd in the metallenes and Pd/C was dominant in its metallic state, along with a few Pd^{2+} species due to slight surface oxidation (Fig. 2b). Of note is that Pd–Mo afforded the visible blue-shift of Pd $3d_{3/2}$ and $3d_{5/2}$ to higher binding energies in

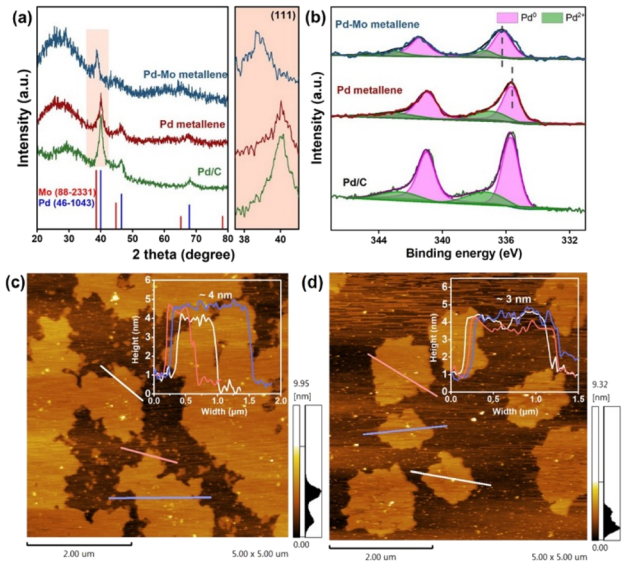

Fig. 2 (a) XRD patterns and (b) Pd core-level XPS profiles of commercial Pd/C, the Pd metallene, and the Pd–Mo metallene. AFM images and the corresponding height profiles of (c) Pd and (d) Pd–Mo metallenes.

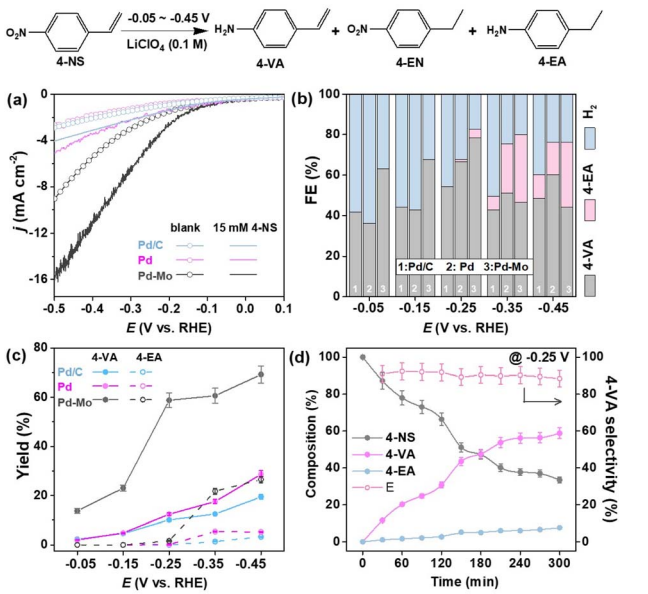

Fig. 3 ECH performance of 4-NS over Pd-based metallenes. (a) Polarization curves of Pd–Mo and Pd metallenes and commercial Pd/C in 0.1 M $LiClO_4$ with and without 15 mM of 4-NS at a scan rate of 10 mV s^{-1}. (b) FEs and (c) yields of products for the ECH of 4-NS over Pd-based metallenes and commercial Pd/C in a wide potential range of −0.05 to −0.45 V *vs.* RHE (4-NS: 15 mM, reaction time: 5 h). (d) Time curves of 4-NS, 4-VA and 4-EA on the Pd–Mo metallene at −0.25 V *vs.* RHE.

comparison with the Pd metallene and Pd/C, associated with the strong electronic interactions between Mo and Pd after alloying. Accordingly, the XPS profile of Mo 3d (Fig. S3, ESI†) showed the presence of Mo^0 in nanosheets, which increased along with reaction time. The binding energies of 227.6 eV ($3d_{5/2}$) and 229.8 eV ($3d_{3/2}$) were obviously lower than the typical values of Mo metal (228.0 and 231.0 eV).[38] As indicated, Mo is negatively charged after alloying due to the electron donation by Pd, in accordance with the XPS profile of Pd (Fig. 2b) and the follow-up DFT calculation. In addition, AFM measurement was conducted to evaluate the ultrathin 2D nanostructure. As shown in Fig. 2c and d, Pd and Pd–Mo metallenes possessed a consistent thickness of 3–4 nm, which implied the negligible influences on morphology by alloying Pd with Mo atoms.

Prior to electrocatalytic tests, Pd-based metallenes were electrochemically cleaned by repeated CVs. The significantly improved current densities on Pd and Pd–Mo suggested the successful removal of adsorbed surfactants (Fig. S4, ESI†).[36] Then, the CVs of Pd–Mo were measured in 0.1 M $LiClO_4$ (pH 6.8) containing 10 mmol L^{-1} of 4-NS (Fig. S5, ESI†), which showed a new cathodic peak at 0.05 V *vs.* RHE corresponding to the stepwise reduction of nitro.[39,40] Such cathodic reduction of 4-NS before the HER confirms its thermodynamic priority, in which electrons can be used to reduce nitroarenes with chemisorbed H* or *via* a proton-coupled-electron transfer (PCET) process.[18,41] The reduction of 4-NS can produce 4-VA and 4-ethylnitrobenzene (4-EN) *via* selectively hydrogenating nitro and vinyl groups, respectively, both of which would be further reduced to 4-EA.[42] Because of the more thermodynamically preferred reduction of nitro to vinyl, the production of 4-EN is usually prohibited.[43] Fig. 3a presents the linear sweep voltammetry curves of Pd–Mo and Pd metallenes, along with the reference of commercial Pd/C. The cathodic currents of all three catalysts increased after introducing 4-NS, confirming again the favourable reduction in comparison with the HER. Among these electrocatalysts, Pd–Mo delivered the highest current with 4-NS, implying the best activity for hydrogenation.

Afterwards, electrocatalytic tests were carried out at −0.05 to −0.45 V *vs.* RHE for 5 h, in a 0.1 M $LiClO_4$ solution containing 15 wt% methanol to improve the solubility of 4-NS (15 mM). HPLC clearly identified the conversion of 4-NS to the target 4-VA and 4-EA by-product (Fig S6, ESI†). As shown in Fig. 3b, the Pd–Mo metallene gained the FE of 4-VA > 60.0% at −0.05 V and −0.15 V *vs.* RHE, obviously higher than those on Pd and Pd/C counterparts (~40.0%), which identified the more favourable ECH of 4-NS than the HER over Pd–Mo. The FE of 4-VA on Pd–Mo increased to 78.3% at −0.25 V *vs.* RHE, with a low FE of 4-EA (4.5%). At more negative potentials (*e.g.*, −0.35 and −0.45 V *vs.* RHE), Pd–Mo delivered a visibly decreased FE of 4-VA owing to the over-hydrogenation, but it still retained a high FE (~80.0%) for 4-NS reduction. As indicated, the hydrogenation of vinyl in 4-VA is favored at more negative potentials, where the reduction of either nitro or vinyl exceeds H_2 evolution. Remarkably, the control of ECH pathways can be achieved by easily controlling working potentials,[44] and to produce more valuable 4-VA, the electrolysis should proceed above −0.25 V *vs.* RHE. Fig. 3c further summarizes the yields of 4-VA and 4-EA over these electrocatalysts at −0.05 to −0.45 V *vs.* RHE. Visibly, Pd–Mo presented a higher yield of 4-VA in comparison with the Pd metallene and commercial Pd/C, confirming its superiority in ECH. Although the yield of 4-EA increased at −0.35 and −0.45 V

vs. RHE, the yield of target 4-VA remained at a high level. The above results clearly pointed out the advantages of the Pd–Mo metallene with a highly exposed active surface. More importantly, the alloying promotion in ECH was underscored by directly comparing the performance of Pd–Mo and Pd metallenes that possess consistent nanostructures. In further comparison with recently reported electrocatalysts used for 4-NS reduction (Table S3†), the Pd–Mo metallene performed among the best, and featured mild operation with near-neutral electrolytes, avoiding the use of corrosive acids and alkalis.

Fig. 3d displays the electrocatalytic conversion of 4-NS to 4-VA and 4-EA on the Pd–Mo metallene at −0.25 V *vs.* RHE as a function of time. The concentration of 4-NS decreased rapidly during electrolysis, and the target product of 4-VA accordingly increased, while the by-product of 4-EA remained at a low level, resulting in a high selectivity (>90.0%) of 4-VA. This indicated the highly selective hydrogenation of nitro rather than vinyl groups at this moderately negative potential, owing to the preferred activation of nitro groups on Pd sites *via* perpendicular chemisorption.[45] Moreover, the robust service life of Pd–Mo electrocatalysts could be confirmed by 5 successive tests at −0.25 V *vs.* RHE (Fig. S7, ESI†), which showed the well-remained FE and yield of 4-VA. Accordingly, the spent Pd–Mo metallene verified the structural and chemical stability satisfactory for the ECH, according to TEM, XRD, and XPS results (Fig. S8 and S9, ESI†).

Quasi *in situ* EPR measurement coupled with the electrochemical test was conducted to detect the active species during reduction. 5,5-dimethyl-1-pyrroline-*N*-oxide (DMPO) as a trapping agent was introduced into the electrolyte. As shown in Fig. 4a, the characteristic EPR signals of DMPO-H adducts (nine peaks, $\alpha_N = 16.5$ G and $\alpha_H = 22.6$ G) were visible at −0.25 V *vs.* RHE, which suggested that the active H* species for 4-NS hydrogenation was produced *via* water reduction.[46,47] Pd-based electrocatalysts are capable of reducing the free-energy barrier of a Volmer step in a neutral aqueous solution due to their strong binding with H_2O, leading to the rapid generation of H* species on the surface.[48] The successful trapping of hydrogen radicals is associated with the spillover and diffusion of H* on the Pd–Mo surface, consistent with the larger H region and the more negative potential of H_2O reduction on Pd–Mo compared with the Pd metallene (Fig. S10, ESI†).

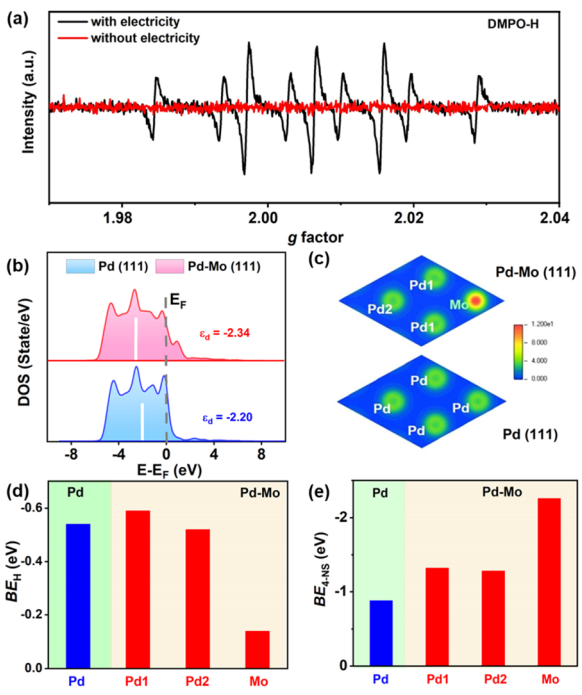

Fig. 4 (a) Quasi *in situ* EPR trapping of hydrogen radicals over Pd–Mo metallene. (b) PDOS for the d band of Pd and PdMo, and (c) electron density difference with Pd (111) and Pd–Mo (111). (d) BE_H and (e) $BE_{4\text{-}NS}$ on Pd (111) and Pd–Mo (111).

We carried out DFT calculation to analyse the electronic configurations and binding energies of H* and 4-NS* on crystal models. The facets of Pd(111) and Pd–Mo(111) were adopted as the calculation models because they were commonly observed in TEM. Fig. 4b depicts the projected density of states (PDOS) for the d bands of Pd(111) and Pd–Mo(111). The d-band of Pd–Mo was visibly broadened as compared with pristine Pd, suggesting electron redistribution after alloying with Mo. Accordingly, the d-band centre (ε_d) slightly downshifted away from the E_F from −2.20 eV (Pd) to −2.34 eV (Pd–Mo). Meanwhile, the electron density difference diagram showed that electrons on the (111) facet were concentrated around Mo atoms in Pd–Mo, while the distribution was uniform in Pd(111) (Fig. 4c). This can be used to explain the shift of Pd 3d and Mo 3d binding energies in the XPS profile of the Pd–Mo metallene (Fig. 2b and S3, ESI†). As highlighted in previous reports,[49,50] tuning electron distribution is feasible to engineer the energetics of reaction intermediates in electrocatalysis. Fig. 4d and e show the binding energies of H* (BE_H) and 4-NS* ($BE_{4\text{-}NS}$) on Pd(111) and Pd–Mo(111), whose adsorption configurations were accordingly summarized in Fig. S11, ESI.† A linear relationship of binding energies with ε_d has been previously proved on the metal surface;[51,52] however, BE_H is still correlated with adsorption sites, in particular on an alloy surface with multiple metal atoms. Such a difference associated with adsorption sites has been examined in this work. Of note, the charge redistribution in Pd–Mo results in positively charged Pd, which enables the Pd site close to Mo (Pd1 in Fig. 4d) with a relatively higher BE_H compared to metallic Pd, and another site (Pd2) with a similar value. By contrast, the negatively charged Mo sites exhibit weak BE_H. The alloying of Mo would strengthen the chemisorption of H* on adjacent Pd sites, which is conducive to stabilizing reactive H* for subsequent hydrogenation. Moreover, the $BE_{4\text{-}NS}$ on the Pd1 and Pd2 sites was obviously increased on Pd–Mo in comparison with Pd and reached the maximum at the Mo site (Fig. 4e). The Mo with relatively stronger oxyphilicity than Pd favours the strong binding with a nitro group, which is of great importance for its activation toward efficient reduction. Taking both BE_H and $BE_{4\text{-}NS}$ into account, we can assume that the adjacent atoms of Pd and Mo would serve as the active sites to chemisorb H* and 4-NS* intermediates, respectively, which subsequently undergo the surface steps of consecutive hydrogenation *via* a typical Langmuir–Hinshelwood mechanism.

Via the same synthetic approach with $Cr(CO)_6$, $Mo(CO)_6$, or $W(CO)_6$ as reactants, a family of Pd–M (M = Cr, Mo and W)

metallenes can be successfully achieved, which serves as a reliable platform to acquire further insights into the alloying promotion of ECH. Their XRD patterns are summarized in Fig. 5a. In comparison with Pd, Pd–W and Pd–Mo showed the obvious shift of the (111) peak to lower 2θ, but Pd–Cr presented the opposite move to a higher degree, associated with the order of atomic radius, *i.e.*, Cr (1.29 Å) < Pd (1.37 Å) < Mo (1.40 Å) < W (1.41 Å). The alloying of Pd with secondary metals (Cr, Mo, and W) leads to lattice contraction or expansion relying on their different atomic sizes. It's further identified by TEM that 2D nanostructures with varied sizes were harvested in these Pd–M samples (Fig. S12, ESI†). To evaluate the exposure of surface active sites, the electrochemical surface area (ECSA) of Pd–M was taken for comparison. The ECSA values of Pd, Pd–Cr, Pd–Mo, and Pd–W metallenes were 111.60, 100.41, 123.46, and 129.71 cm^2 mg^{-1}, respectively, calculated from the cathodic peak of PdO reduction in CVs (Fig. S13 and Table S4, ESI†).

DFT calculations on Pd–M showed that the PDOS near the E_F increased after introducing Mo or W atoms, but decreased with Cr (Fig. 4b). The ε_d downshifted away from the E_F in the order of Pd–W (−2.47 eV) < Pd–Mo (−2.34 eV) < Pd (−2.20 eV) < Pd–Cr (−2.18 eV). Accordingly, the $BE_{4\text{-NS}}$ increased with the alloying of Cr, Mo, and W, in the order of Pd–Mo > Pd–W > Pd–Cr > Pd (Fig. 5c and S12, ESI†), indicating that the oxygen-philic elements of Cr, Mo, and W would enhance the adsorption/activation of nitro substrates.[14] It's more interesting that the specific rate ($r_{4\text{-NS,ECSA}}$) of 4-NS hydrogenation in 1 h electrolysis normalized by the ECSA was closely correlated with the order of $BE_{4\text{-NS}}$ on Pd–M, pointing out the dominant contribution of nitro activation due to its high energy barrier.[9,45] Therefore, the alloying promotion of Pd–M metallenes can be intrinsically ascribed to the strengthened chemisorption of 4-NS*.[23] As schematically illustrated in Fig. 5d, the strong adsorption of 4-NS on oxygenphilic M centres helps in the activation of nitro groups, and in the meantime the available H* on the neighbour Pd sites is conducive to attacking the activated nitro group for further hydrogenation, leading to the facilitated ECH kinetics. The vertical chemisorption of 4-NS on Pd–M *via* bonding nitro with M sites would enable the highly selective reduction towards 4-VA with a well-retained vinyl.

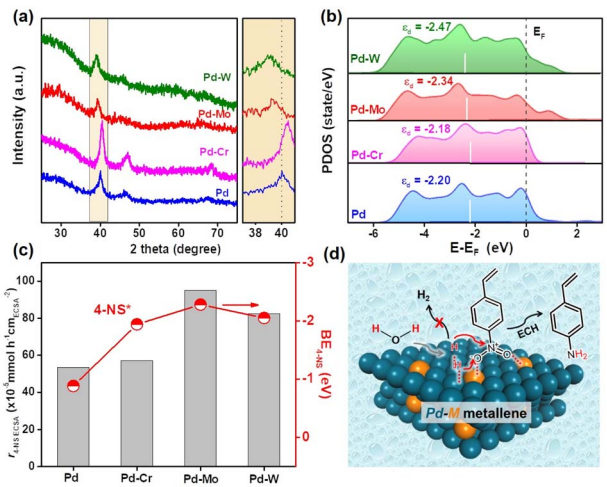

Fig. 5 (a) XRD patterns of Pd, Pd–Cr, Pd–Mo, and Pd–W metallenes. (b) PDOS for the d band of Pd and Pd–M (M = Cr, Mo, and W). (c) Specific reaction rate of 4-NS on Pd and Pd–M metallenes plotted against $BE_{4\text{-NS}}$. (d) Schematic illustration of the ECH mechanism of 4-NS.

Table 1 ECH of various functionalized nitroarenes over the Pd–Mo metallene

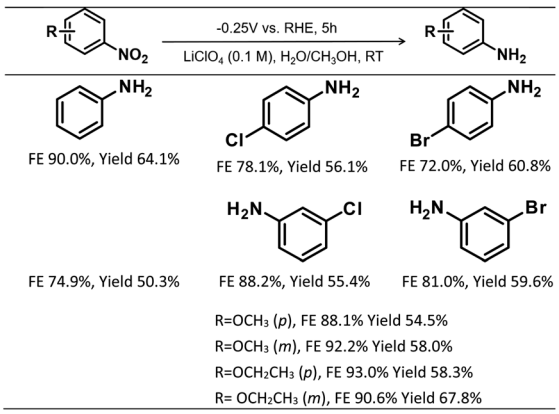

Finally, we examined the efficacy of the Pd–Mo metallene for the electrochemical reduction of a series of nitro compounds (Table 1). For nitrobenzene, the FE and yield of aniline were 90.0% and 64.1% on the Pd–Mo metallene, respectively, in which the byproducts of phenylhydroxylamine and H_2 were rarely detected. In comparison, the yield (50.3–60.8%) and FE (72.0–88.2%) of target aniline derivatives were decreased for halogenated nitrobenzenes, due to the weakened π coupling between nitro and the benzene ring due to electron-withdrawing halogens. Accordingly, the electron-donating alkoxy groups favoured the ECH of nitro with high FE. These results verify the Pd–Mo metallene as a promising catalyst for the ECH of nitroarenes.

Conclusions

In this work, a series of Pd-based metallenes are for the first time introduced as efficient electrocatalysts for the ECH of nitro compounds, in which the alloying promotion has been well identified. Thanks to the highly exposed surface and strong electronic interactions between Pd and Mo atoms, the ultrathin Pd–Mo metallene enables the chemoselective hydrogenation of 4-NS to value-added 4-VA in a wide potential range of −0.05 to −0.45 V *vs.* RHE, superior to the Pd metallene and commercial Pd/C. The consistent alloying promotion is further verified on Pd–M (M = Cr, Mo, and W) metallenes, with a specific activity sequence of Pd–Mo > Pd–W > Pd–Cr > Pd, which is highly correlated with the strengthened chemisorption of 4-NS* after alloying Pd with M. It is expectable that precise control over the alloying effects on binary, ternary, quaternary, and even high-entropy metallene platforms could further boost electrocatalytic applications.

Author contributions

Wenbiao Zhang: synthesis, investigations, methodology, DFT calculation, data curation, writing – original draft. Wanling Zhang: synthesis, data validation. Jingwen Tan: EPR testing. Di Pan: experimental analysis. Yi Tang: conceptualization, supervision, funding acquisition. Qingsheng Gao: conceptualization, supervision, writing – review and editing, funding acquisition.

Conflicts of interest

The authors declare no competing financial interest.

Acknowledgements

This work was financially supported by the National Key Research and Develoment Program of China (2018YFA0209402), National Natural Science Foundation of China (22175077, 22088101, and 22072028), Innovation Team Project in Guangdong Colleges and Universities (2021KCXTD009), and Guangzhou Science and Technology Program (202201020071).

Notes and references

1 J. Yang, H. Qin, K. Yan, X. Cheng and J. Wen, *Adv. Synth. Catal.*, 2021, **363**, 5407–5416.
2 S. A. Akhade, N. Singh, O. Y. Gutierrez, J. Lopez-Ruiz, H. Wang, J. D. Holladay, Y. Liu, A. Karkamkar, R. S. Weber, A. B. Padmaperuma, M. S. Lee, G. A. Whyatt, M. Elliott, J. E. Holladay, J. L. Male, J. A. Lercher, R. Rousseau and V. A. Glezakou, *Chem. Rev.*, 2020, **120**, 11370–11419.
3 P. Zhang and L. Sun, *Chin. J. Chem.*, 2020, **38**, 996–1004.
4 B. Huang, Z. Sun and G. Sun, *eScience*, 2022, **2**, 243–277.
5 P. Serna and A. Corma, *ACS Catal.*, 2015, **5**, 7114–7121.
6 P. Lara and K. Philippot, *Catal. Sci. Technol.*, 2014, **4**, 2445–2465.
7 Y. Shu, H. C. Chan, L. Xie, Z. Shi, Y. Tang and Q. Gao, *ChemCatChem*, 2017, **9**, 4199.
8 J. Song, Z.-F. Huang, L. Pan, K. Li, X. Zhang, L. Wang and J.-J. Zou, *Appl. Catal., B*, 2018, **227**, 386–408.
9 Y. Shi, W. Zhang, J. Tan, T. Y. Yan, Y. Jia, Z. Wang, Y. Tang and Q. Gao, *Adv. Mater. Interfaces*, 2022, **9**, 2200505.
10 F. W. Lucas, R. G. Grim, S. A. Tacey, C. A. Downes, J. Hasse, A. M. Roman, C. A. Farberow, J. A. Schaidle and A. Holewinski, *ACS Energy Lett.*, 2021, **6**, 1205–1270.
11 M. Jin, Y. Liu, X. Zhang, J. Wang, S. Zhang, G. Wang, Y. Zhang, H. Yin, H. Zhang and H. Zhao, *Appl. Catal., B*, 2021, **298**, 120545.
12 W. Zhang, Y. Shi, Y. Yang, J. Tan and Q. Gao, *Chin. J. Catal.*, 2022, **43**, 3116–3125.
13 C. J. Bondue, F. Calle-Vallejo, M. C. Figueiredo and M. Koper, *Nat. Catal.*, 2019, **2**, 243–250.
14 J. Tan, J. Shao, Y. Shi, W. Zhang and Q. Gao, *ACS Sustainable Chem. Eng.*, 2022, **10**, 13525–13533.
15 Z. Sun, S. Wang and W. Chen, *J. Mater. Chem. A*, 2021, **9**, 5296–5319.
16 D. Carvajal, R. Arcas, C. A. Mesa, S. Giménez, F. Fabregat-Santiago and E. Mas-Marzá, *Adv. Sustainable Syst.*, 2022, **6**, 2100367.
17 F. Nosheen, N. Wasfi, S. Aslam, T. Anwar, S. Hussain, N. Hussain, S. N. Shah, N. Shaheen, A. Ashraf and Y. Zhu, *Nanoscale*, 2020, **12**, 4219–4237.
18 K. Koh, U. Sanyal, M. S. Lee, G. Cheng, M. Song, V. A. Glezakou, Y. Liu, D. Li, R. Rousseau, O. Y. Gutierrez, A. Karkamkar, M. Derewinski and J. A. Lercher, *Angew. Chem., Int. Ed.*, 2020, **59**, 1501–1505.
19 K. Yao, T. Li, C. Zhao, W. Lu, S. Zhao and J. Wang, *ACS Sustainable Chem. Eng.*, 2020, **8**, 14914–14926.
20 X. Li, P. Shen, X. Li, D. Ma and K. Chu, *ACS Nano*, 2023, **17**, 1081–1090.
21 Y. Gao, Q. Xue, J. Li, M. Zhang, Y. Ma and Y. Qu, *ACS Appl. Mater. Interfaces*, 2022, **14**, 14202–14209.
22 A. D. Stergiou and M. D. Symes, *Cell Rep. Phys. Sci.*, 2022, **3**, 100914.
23 S. Wu, X. Huang, H. Zhang, Z. Wei and M. Wang, *ACS Catal.*, 2022, **12**, 58.
24 M. Luo, Z. Zhao, Y. Zhang, Y. Sun, Y. Xing, F. Lv, Y. Yang, X. Zhang, S. Hwang, Y. Qin, J. Y. Ma, F. Lin, D. Su, G. Lu and S. Guo, *Nature*, 2019, **574**, 81–85.
25 H. Xu, H. Shang, C. Wang and Y. Du, *Small*, 2021, **17**, e2005092.
26 F. Lv, B. Huang, J. Feng, W. Zhang, K. Wang, N. Li, J. Zhou, P. Zhou, W. Yang, Y. Du, D. Su and S. Guo, *Natl. Sci. Rev.*, 2021, **8**, nwab019.
27 H. Q. Ta, R. G. Mendes, Y. Liu, X. Yang, J. Luo, A. Bachmatiuk, T. Gemming, M. Zeng, L. Fu, L. Liu and M. H. Rümmeli, *Adv. Sci.*, 2021, **8**, 2100619.
28 J. Zhang, F. Lv, Z. Li, G. Jiang, M. Tan, M. Yuan, Q. Zhang, Y. Cao, H. Zheng, L. Zhang, C. Tang, W. Fu, C. Liu, K. Liu, L. Gu, J. Jiang, G. Zhang and S. Guo, *Adv. Mater.*, 2022, **34**, 2105276.
29 F. Lin, F. Lv, Q. Zhang, H. Luo, K. Wang, J. Zhou, W. Zhang, W. Zhang, D. Wang, L. Gu and S. Guo, *Adv. Mater.*, 2022, **34**, 2202084.
30 J. Wu, X. Zhao, X. Cui and W. Zheng, *Chin. J. Catal.*, 2022, **43**, 2802–2814.
31 J. Wu, J. Fan, X. Zhao, Y. Wang, D. Wang, H. Liu, L. Gu, Q. Zhang, L. Zheng, D. J. Singh, X. Cui and W. Zheng, *Angew. Chem., Int. Ed.*, 2022, **61**, e202207512.
32 X. Li, P. Shen, Y. Luo, Y. Li, Y. Guo, H. Zhang and K. Chu, *Angew. Chem., Int. Ed.*, 2022, **61**, e202205923.
33 K. Chen, Z. Ma, X. Li, J. Kang, D. Ma and K. Chu, *Adv. Funct. Mater.*, 2023, **33**, 2209890.
34 W. Zhong, B.-Q. Miao, M.-Y. Wang, Y. Ding, D.-S. Li, S.-B. Yin, X.-F. Li and Y. Chen, *J. Mater. Chem. A*, 2022, **10**, 20343–20349.
35 Y. Yang, Y. Shu, Y. Wu and Q. Gao, *Chem. Eng. J.*, 2021, **425**, 131858.
36 Y. Wu, J. Zeng, Y. Yang, Z. Li, W. Zhang, D. Li and Q. Gao, *Mater. Chem. Front.*, 2021, **5**, 4327–4333.
37 W. C. Sheng, S. Kattel, S. Y. Yao, B. H. Yan, Z. X. Liang, C. J. Hawxhurst, Q. Y. Wu and J. G. G. Chen, *Energy Environ. Sci.*, 2017, **10**, 1180–1185.

38 E. Minni and F. Werfel, *Surf. Interface Anal.*, 1988, **12**, 385–390.
39 H. Salehzadeh and M. H. Mashhadizadeh, *J. Org. Chem.*, 2019, **84**, 9307–9312.
40 F. Li, R. Meng, W. Wang, W. Wang and B. Jin, *J. Phys. Chem. C*, 2021, **125**, 16464–16472.
41 S. C. Jensen, S. Bettis Homan and E. A. Weiss, *J. Am. Chem. Soc.*, 2016, **138**, 1591–1600.
42 Y. Ren, C. Hao, Q. Chang, N. Li, J. Yang and S. Hu, *J. Mater. Chem. A*, 2021, **9**, 25374–25380.
43 L. Li, Y. Li, L. Jiao, X. Liu, Z. Ma, Y.-J. Zeng, X. Zheng and H.-L. Jiang, *J. Am. Chem. Soc.*, 2022, **144**, 17075–17085.
44 X. Chong, C. Liu, Y. Huang, C. Huang and B. Zhang, *Natl. Sci. Rev.*, 2020, **7**, 285–295.
45 Y. Sun, A. J. Darling, Y. Li, K. Fujisawa, C. F. Holder, H. Liu, M. J. Janik, M. Terrones and R. E. Schaak, *Chem. Sci.*, 2019, **10**, 10310–10317.
46 M. Li, C. Liu, Y. Huang, S. Han and B. Zhang, *Chin. J. Catal.*, 2021, **42**, 1983–1991.
47 J. Tan, W. Zhang, Y. Shu, H. Lu, Y. Tang and Q. Gao, *Sci. Bull.*, 2021, **66**, 1003–1012.
48 Y. Gao, R. Yang, C. Wang, C. Liu, Y. Wu, H. Li and B. Zhang, *Sci. Adv.*, 2022, **8**, eabm9477.
49 J. Zeng, W. Zhang, Y. Yang, D. Li, X. Yu and Q. Gao, *ACS Appl. Mater. Interfaces*, 2019, **11**, 33074–33081.
50 Z. Zhao and G. Lu, *J. Mater. Chem. A*, 2020, **8**, 12457–12462.
51 H. Xin, A. Vojvodic, J. Voss, J. K. Nørskov and F. Abild-Pedersen, *Phys. Rev. B*, 2014, **89**, 115114.
52 Q. Gao, W. Zhang, Z. Shi, L. Yang and Y. Tang, *Adv. Mater.*, 2019, **31**, 1802880.